1 # H_3PO_4 activation mediated the iron phase transformation and enhanced the

2 # removal of bisphenol A on iron carbide-loaded activated biochar

3 Nan Zhao [a,b], Kunyuan Liu [a], Chao He [a], Dongye Zhao [c], Ling Zhu [d], Chuanfang Zhao [e],

4 Weihua Zhang [a,b], Wen-Da Oh [f], Weixian Zhang,[d,g] Rongliang Qiu [a,g,h*]

5 [a] *School of Environmental Science and Engineering, Sun Yat-sen University, Guangzhou 510275, PR*

6 *China*

7 [b] *Guangdong Provincial Key Lab of Environmental Pollution Control and Remediation Technology,*

8 *Sun Yat-sen University, Guangzhou 510275, PR China*

9 [c] *Department of Civil & Environmental Engineering, Auburn University, Auburn, AL 36849, USA*

10 [d] *State Key Laboratory of Pollution Control and Resource Reuse, College of Environmental Science*

11 *and Engineering, Tongji University, Shanghai, 200092, PR China*

12 [e] *Research Center for Eco-Environmental Sciences, Chinese Academy of Sciences, Beijing 100085,*

13 *PR China*

14 [f] *School of Chemical Sciences, Universiti Sains Malaysia, 11800 Penang, Malaysia*

15 [g] *Guangdong Laboratory for Lingnan Modern Agriculture, Guangzhou 510642, PR China*

16 [h] *Guangdong Provincial Key Laboratory of Agricultural & Rural Pollution Abatement and*

17 *Environmental Safety, College of Natural Resources and Environment, South China Agricultural*

18 *University, Guangzhou 510642, PR China*

19

20

21

22 *Corresponding authors

23 Tel: +86 20 84113454

24 E-mail address: eesqrl@mail.sysu.edu.cn

25

26

27

ABSTRACT

Zero valent iron-loaded biochar (Fe^0-BC) has shown promise for the removal of various organic pollutants, but is restricted by reduced specific surface area, low utilization efficiency and limited production of reactive oxygen species (ROS). In this study, iron carbide-loaded activated biochar (Fe_3C-AB) with a high surface area was synthesized through the pyrolysis of H_3PO_4 activated biochar with $Fe(NO_3)_3$, tested for removing bisphenol A (BPA) and elucidated the adsorption and degradation mechanisms. As a result, H_3PO_4 activated biochar was beneficial for the transformation of Fe^0 to Fe_3C. Fe_3C-AB exhibited a significantly higher removal rate and removal capacity for BPA than that of Fe^0-BC within a wide pH range of 5.0–11.0, and its performance was maintained even under extremely high salinity and different water sources. Moreover, X-ray photoelectron spectra and density functional theory calculations confirmed that hydrogen bonds were formed between the COOH groups and BPA. $^1O_2$ was the major reactive species, constituting 37.0% of the removal efficiency in the degradation of BPA by Fe_3C-AB. Density functional reactivity theory showed that degradation pathway 2 of BPA was preferentially attacked by ROS. Thus, Fe_3C-AB with low cost and excellent recycling performance could be an alternative candidate for the efficient removal of contaminants.

Keywords: H_3PO_4 activation; Fe_3C-loaded activated biochar; hydrogen bond; singlet oxygen degradation; degradation pathway

1. Introduction

Bisphenol A (BPA) is a persistent endocrine disrupting chemical, and has been associated with various types of heart disease and cancer (vom Saal and Hughes, 2005). BPA can accumulate along the food chain and has been widely detected in wastewater and surface waters (Belfroid et al., 2002; Yang et al., 2018). More seriously, it was

detected in the human blood and tissues (vom Saal and Hughes, 2005). Thus, the European Food Safety Authority (EFSA) reduced the tolerable daily intake to 4 µg/kg body weight/day in 2015 (EFSA, 2016).

Adsorption is deemed an effective, low-cost, and well-established treatment method for organic pollutant removal. To this end, biochar has been widely investigated as an adsorbent from inexpensive feedstocks (Kumar et al., 2020; Wang et al., 2019; Zhao et al., 2020). However, the adsorption performance of conventional biochar remains limited owing to its low specific surface area and unfavorable physicochemical characteristics (Zhao et al., 2017). Zero-valent iron (Fe^0) has been used to combine adsorption and reductive degradation for removing organic pollutants (Cuervo Lumbaque et al., 2019). It could also be applied as a source of non-photochemical reactive oxygen species (ROS) to degrade pharmaceutically active compounds. However, Fe^0 is prone to oxidation and surface passivation (Pang et al., 2019), which causes insufficient ROS concentration and poor recycling performance. To overcome these drawbacks, Fe/C composites have been increasingly studied as they exhibit superior properties compared to individual materials, such as improved reactivity, stability, and environmental safety and reduced toxicity (Kumar et al., 2020; Liang et al., 2019). Moreover, they integrate adsorption, complexation, and reduction and show improved removal and degradation of organic pollutants (Sun et al., 2019). In this regard, Fe^0 has been most commonly used for modifying biochar.

Fe^0-magnetite loaded biochar (ZVI-MBC) has been studied to treat pentachlorophenol (PCP), chloramphenicol, trichloroethylene, and trichloromethane through adsorption and reductive degradation (Ahmed et al., 2017; Devi and Saroha, 2014; Qian et al., 2020). The dissolution of H_2O molecules by Fe^0 caused the production of H_2 and then formed atomic H. Atomic H could degrade PCP through

78 reduction to remove chloride. Fe^0 could also activate O_2 to form H_2O_2, $^\bullet OH$ and $^\bullet O_2^-$ for

79 the oxidation degradation of PCP and these ROS were responsible for the

80 mineralization of PCP (Shih et al., 2016). However, *in situ* adsorption and oxidative

81 degradation, without adding oxidants for removing organic contaminants, were rarely

82 reported.

83   Fe^0-BC has magnetic property, which is easily separated and recycled in the

84 practical application for the treatment of real wastewater. But, its removal capacity will

85 be affected because the material was susceptible to suffer from surface passivation in

86 the existence of O_2 and H_2O (Devi and Saroha, 2014). For $Fe^0/Fe_3C/C$ composite,

87 Fe_3C/C could protect the Fe^0 core against oxidization and maintain excellent stability

88 during the removal of pollutant. Li et al. also indicated that Fe/C system had low

89 utilization efficiency as compared to $Fe^0/Fe_3C/C$ composite because Fe_3C could

90 improve the electron tunneling efficiency between Fe^0 and the graphitic shell (Li et al.,

91 2019). Meanwhile, Fe^0-BC has a small surface area and pore volume due to pore

92 blocking. For example, the surface area of ZVI-MBC is 101 m^2/g (Devi and Saroha,

93 2014), which limits their adsorption capacity for organic contaminants. To increase the

94 surface area, the chemical activation of biochar has been employed using various

95 chemical modification reagents, including alkalis (NaOH, KOH, and NH_3), mineral

96 salts (MnO_x, $FeCl_3$ and $ZnCl_2$), and acids (H_2SO_4, H_3PO_4, and HCl) (Fierro et al., 2006;

97 Mohan and Pittman 2006; Yao et al., 2018). These modification reagents can also

98 change the physicochemical properties, graphitization degree, morphology, and surface

99 chemistry of biochars, then affect the affinity between carbon matrix and loaded Fe^0 as

100 well as the catalytic activity of biochar (Li et al., 2020; Yang et al., 2019). Although the

101 simultaneous activation by using $FeCl_3$ and $ZnCl_2$ enlarged the surface area and

102 promoted the formation of Fe_3C and graphite (Yao et al., 2018), the existence of Fe_3O_4

103   in $Fe_3C/Fe_3O_4/C$ nanosheets might reduce the reactivity of the materials and $ZnCl_2$

104   could induce toxicity concerns. Thus, it is important to regulate the complete reduction

105   of Fe_3O_4 to Fe^0.

106   H$_3$PO$_4$ activated biochar has been wildly used to increase the removal capacity of

107   pollutants (Chen et al., 2018; Puziy et al., 2020; Zhao et al., 2017). H_3PO_4, is

108   inexpensive, harmless, and effective in increasing the surface area and carbonization of

109   biochar (Zhao et al., 2017). And, the formed amorphous carbon is beneficial for

110   converting Fe_2O_3 and Fe_3O_4 to Fe^0 and can react with Fe species to form Fe_3C (Yao et

111   al., 2018; Zeng et al., 2021). Thus, H_3PO_4 activated biochar was used as the host

112   material for iron carbide (Fe_3C). Fe_3C-loaded activated biochar (Fe_3C-AB) was

113   synthesized and tested for its potential in removing BPA from aqueous solutions. The

114   specific objectives were to 1) explore the formation mechanism of Fe_3C-AB, 2)

115   investigate the BPA removal kinetics of Fe_3C-AB and compare with Fe^0-BC, 3) examine

116   the effects of various critical parameters (initial concentration, pH, ion strength, and

117   water sources) on the removal performance, and 4) elucidate the removal mechanisms

118   and degradation pathways using experimental and theoretical calculation method.

119   **2. Materials and methods**

120   *2.1. Preparation of Fe_3C-AB and Fe^0-BC*

121   The preparation of biochar and H_3PO_4 activated biochar were depicted in the

122   supplementary material. Fe^0-BC and Fe_3C-AB were prepared by thermal reduction

123   method (Zhang et al., 2019). Fe^0-BC was synthesized under N$_2$ atmosphere with a flow

124   rate of 25 cm^3/min, by mixing 400 mg of the untreated biochar (without the acid

125   pre-treatment) with $Fe(NO_3)_3·9H_2O$ (800 mg) in 50 mL of high purity water. The pH

126   was adjusted to 4.0 using 0.1 M HNO$_3$ to prevent hydrolysis. After stirring at room

127   temperature for 7 h, the mixture was dried at 105 ℃ for 48 h. The dried mixture was

128 transferred to a tube furnace and pyrolyzed at 600 ℃ for 2 h (10 ℃/min). Fe$_3$C-AB was

129 synthesized following the same process, except that H$_3$PO$_4$ activated biochar was used.

130 The biochar and H$_3$PO$_4$ activated biochar pyrolyzed at 600°C without the addition of Fe

131 salt were used as the control samples and denoted as BC and AB. Finally, the resulting

132 Fe/C materials were ground and sieved through a 100-mesh screen, and those that

133 passed the screen were used in this study. The Fe contents in Fe^0-BC and Fe$_3$C-AB were

134 20.3% and 27.7%, respectively. The free iron and dissolved organic matter of Fe/C

135 composites were not removed before the BPA removal experiments. The releasing

136 concentrations of free iron when Fe/C composites reacted with high purity water for 24

137 h were 8-9.3 µg/L.

138 *2.2. BPA removal kinetic experiments*

139 Batch kinetic experiments were carried out to determine the removal kinetics of

140 BPA by the prepared Fe/C composites. The tests were initiated by adding 12 mg of a

141 given Fe/C composite into 15 mL of a BPA solution (50 mg/L) in 50 mL brown glass

142 tubes. The mixtures were then shaken at 180 rpm and at 25 ± 1 ℃. At pre-determined

143 times (0, 50, 150, 240, 480, 720, and 1440 min), the mixtures were sampled and

144 centrifuged at 3000 rpm for 5 min, and the supernatant was collected and filtered

145 through a 0.22 µm polytetrafluoroethylene membrane. The filtrates were then analyzed

146 for BPA using ultraviolet–visible (UV–Vis) spectroscopy at 276 nm. Control

147 experiments were also performed with the materials only or with BPA only to exclude

148 the effect of impurities or natural organic matters on the absorbance and adsorption to

149 the vials. All the experiments were conducted in duplicate. The removal amounts of

150 BPA on Fe/C composites were calculated by Eq. (1)

151 $$q_e = V(C-C_e)/m \qquad (1)$$

152 q_e is the removal amount, V is the solution volume, C is initial concentration of BPA, C_e

153   is equilibrium concentration, and *m* is the mass of Fe/C composites.

3.   Results and discussion

3.1. Characterization of Fe₃C-AB and Fe⁰-BC

156   The crystalline phases of the samples were examined via X-ray diffraction analysis

157   (XRD). The diffraction peaks at 44.7º, 65.0º, and 82.3º corresponded to the (110), (200),

158   and (211) planes of Fe^0, respectively (Fig. S1a). The peaks at 37.6º, 42.9º, 43.8º, 44.6º,

159   45.0º, 45.9º, 51.8º, 54.4º, and 74.5º corresponded to the (210), (211), (102), (220), (031),

160   (112), (122), (040), and (400) planes of Fe_3C, respectively (Fig. S1b). In addition, the

161   peaks of Fe^0 were also present. During the carbothermic reduction process, carbon

162   atoms could diffuse into bulk iron until saturation, which could lead to iron

163   nanoparticles being gradually encapsulated by H_3PO_4 activated biochar to form Fe_3C at

164   600^oC under N_2 atmosphere. Moreover, it is noted that the H_3PO_4 activated biochar had

165   a higher carbon content (69.0%) than untreated biochar (60.2%), which could promote

166   the crystallization and growth of the graphite shell. Therefore, Fe_3C was formed on the

167   outer layer of Fe^0 during the formation of the graphite shell (Wan et al., 2020; Yan et al.,

168   2013). To further analyze the formation of Fe₃C-AB in this study, the XRD patterns of

169   the untreated and H_3PO_4 activated biochars pyrolyzed at 600 ^oC without Fe species were

170   also obtained (Fig. S1c and S1d). For the untreated biochar, the pyrolyzed crystalline

171   product was determined to be SiO_2, while for the H_3PO_4 activated biochar, a wide peak

172   centered at 25.5º suggested the presence of amorphous carbon (Li et al., 2018).

173   Therefore, it can be inferred that the H_3PO_4 pre-treatment eliminated SiO_2 and promoted

174   the formation of amorphous carbon because the integration of H_3PO_4 towards the

175   internal surface of corn straw increased the graphitization of biochar (Guediri et al.,

176   2020), however the graphitization was light.

177   Fig. S2 shows the scanning electron microscopy (SEM) images of the Fe/C

178   composites. For Fe^0-BC, a considerable portion of Fe^0 particles were uniformly

179   dispersed and loaded on the surface of the corresponding composites. This phenomenon

180   was not beneficial for the interaction between Fe nanoparticles and char matrix (Fig.

181   S2a). In contrast, for Fe_3C-AB, the Fe_3C particles were partially or completely

182   embedded into the porous char matrix (Fig. S2b), leading to the coverage of the char

183   matrix. Furthermore, Fig. 1 shows the transmission electron microscope (TEM) images.

184   For both Fe^0-BC and Fe_3C-AB, the iron spheres were wrapped in film-like carbon shells

185   with a thickness of 4 and 2.3 nm, respectively. The particle size of the Fe^0 particles in

186   Fe^0-BC ranged from 12 to 88 nm (Fig. 1a), whereas that for Fe_3C was smaller (18–53

187   nm) and more evenly distributed (Fig. 1b). Moreover, the carbon shells of Fe^0-BC

188   appeared amorphous and those of Fe_3C-AB were crystalline (Figs. 1c and 1d), probably

189   due to the H_3PO_4 pre-treatment which promoted the transformation from amorphous

190   carbon to graphitic carbon. Furthermore, the average distance of the interlayer spacing

191   in Fe_3C-AB was 0.34 nm, which conformed to the graphite plane (002) (Wang et al.,

192   2008). The graphitic carbon in Fe_3C-AB was resulted from aromatized and graphitized

193   organic matter in AB. Meanwhile, $Fe(NO_3)_3$ activation could improve the graphitization

194   degree of AB during the pyrolysis process (Zeng et al., 2021; Zhu et al., 2020). In

195   summary, the biochar was modified by iron nanoparticles, which were in turn covered

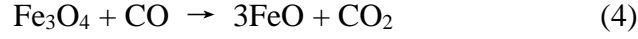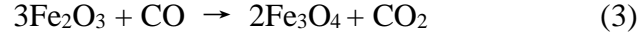196   by a carbonaceous shell, during the pyrolysis process.

197   Fig. S3a shows the N_2 adsorption isotherms for BC, AB, Fe^0-BC and Fe_3C-AB. BC

198   presented very low N_2 adsorption capacity, implying that it was non-porous. The

199   isotherms of AB and Fe_3C-AB belonged to type I pattern, indicating that they were
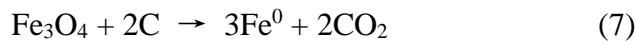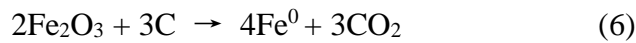
microporous materials and the microporous ratios were as high as 71.0% and 76.6%, respectively (Table S1). The isotherms of Fe^0-BC showed a combination of type IV and I pattern, which suggested the formation of mesopores and micropores (Kruk and Jaroniec, 2001; Tammam et al., 2018; Zhao et al., 2018). The pore size distribution curve (Fig. S3b) also indicated that AB and Fe_3C-AB had porous structures with abundant micropores (Zhao et al., 2017). AB exhibited higher specific surface area of 553 m^2/g and the increased surface area could be attributed to the activation of H_3PO_4, which was indicated by the decrease in the average pore size and the increase in porosity. The abundant pores were beneficial for the entry of $Fe(NO_3)_3$ solution and the reaction of Fe species with the precursor. Thus, the surface area of Fe_3C-AB reduced to 278 m^2/g after loading of Fe_3C and the micropore and mesopore volumes were also reduced, probably because the Fe_3C particles blocked the mesopores and micropores.

To confirm the phase transformation from Fe^0 to Fe_3C after the activation of H_3PO_4, thermogravimetry-mass spectrometry (TG-MS) was conducted and the mass changes of the precursors and outlet gases for BC, AB, Fe^0-BC and Fe_3C-AB were plotted in Fig. S4 and Fig. 2. The weight losses of the precursors for BC and AB were only 36.6% and 21.7% at 600°C, respectively, and more kinds of small molecules were escaped during the pyrolysis process of the precursor for BC than that of AB (Fig. S4). After the Fe impregnation, the mass of the precursor for Fe^0-BC was drastically decreased about 25% up to 300°C because of the evaporation of water molecules (Fig. 2a-b). Meanwhile, the pyrolysis of labile O containing functional groups of BC in 100-300°C yielded CO and CO_2 (Fig. 2b). The reduction of Fe_2O_3 by CO to produce Fe_3O_4 was initiated around 430°C. The next was the reduction of Fe_3O_4, which might occur in 450-500°C. The

thermal decomposition also resulted in a greater mass loss in the temperature 540-600

^oC, indicating that FeO was reduced to Fe^0 (Neeli and Ramsurn, 2018).

$$3Fe_2O_3 + CO \rightarrow 2Fe_3O_4 + CO_2 \qquad (3)$$

$$Fe_3O_4 + CO \rightarrow 3FeO + CO_2 \qquad (4)$$

$$FeO + CO \rightarrow Fe^0 + CO_2 \qquad (5)$$

On the opposite, the precursor in Fe_3C-AB presented different phenomenon. No CO

was detected in the thermal decomposition process. The signal intensity for H_2O was

very weak which could be explained as more water molecules have been removed in the

H_3PO_4 activation process (Fig. 2d). CO_2 in 120-300^oC was produced by the

decomposing of O containing groups in AB. The wide CO_2 peak at 400-500^oC was

assigned to the carbothermal reduction of Fe oxides and the amorphous carbon could

concert Fe_2O_3 and Fe_3O_4 directly to Fe^0. At last, the partial dissolution of carbon into

Fe^0 led to the formation of the well-crystallized Fe_3C particles (Eqs. 6-8; Zeng et al.,

2021):

$$2Fe_2O_3 + 3C \rightarrow 4Fe^0 + 3CO_2 \qquad (6)$$

$$Fe_3O_4 + 2C \rightarrow 3Fe^0 + 2CO_2 \qquad (7)$$

$$3Fe^0 + C \rightarrow Fe_3C \qquad (8)$$

3.2. Removal kinetics of BPA

Fig. 3a shows the removal kinetics of BPA by Fe_3C-AB. A faster initial removal

was observed in the first 240 min, followed by a slow BPA removal process, which

gradually got to the equilibrium after 480 min. About 50.5% of BPA was removed in the

initial 240 min and 58.2% was removed at equilibrium. Fe_3C-AB exhibited higher

removal rate and removal capacity, with an equilibrium removal amount being 2 times

241 greater than that of Fe^0-BC. The pseudo-second order kinetic model best fit the kinetic

242 data (Table S2). The removal rate for Fe_3C-AB was 1.08 mg g^{-1} min^{-1}, which was 32

243 times higher than that of Fe^0-BC. The XRD diffraction peaks of the used samples at

244 $2\theta = 44.7°$ and 35.5° were sharply reduced, indicating the loss of crystalline iron or its

245 involvement in BPA removal (Figs. 3b and 3c), but they still kept their states. However,

246 there was no Fe^0 on the surface of Fe^0-BC after reacting with BPA, as determined by

247 X-ray photoelectron spectroscopy (XPS), indicated that Fe^0-BC was unstable (Figs. S5a

248 and S5b). For Fe_3C-AB, the internal Fe^0 was well protected by the outside Fe_3C and

249 graphite layer (Figs. S5c and S5d).

3.3. Effects of experimental parameters on BPA removal

3.3.1. Initial concentration

252 Fig. 4a and Fig. S6 showed that the removal efficiency of BPA decreased by 46.4%,

253 54.6%, 80.9%, 84.3%, 56.6% and 60.4% when the initial concentrations increased from

254 100-350 mg/L on Fe^0-BC, Fe_3C-AB, Fe^0, Fe_3C, BC and AB, respectively. The marked

255 reduction for the removal efficiency in Fe^0 and Fe_3C systems was because the

256 availability of the sufficient number of ROS was reduced. The existence of carbon

257 matrix in Fe^0-BC and Fe_3C-AB could significantly increase the removal efficiency and

258 provided extra adsorption sites for BPA as compared to pure Fe^0 and Fe_3C. AB had

259 higher removal efficiency than BC because a higher pore volume could lead to a greater

260 removal capacity for BPA (Acostaa et al., 2018; Zhao et al., 2017). Thus, it was the AB

261 supporter made Fe_3C-AB has a higher removal capacity than Fe^0-BC. Fe_3C-AB as a

262 novel Fe/C composite with higher pore volume could be used to effectively remove

263 high concentrations of organic pollutants from contaminated water.

3.3.2. Initial solution pH

265 For Fe^0 and Fe_3C, the highest removal was observed at pH 5.0 and decreased in the

266   following order of pH 5.0 > 8.0 > 11.0 (Fig. 4b). It is noted that Fenton-like processes

267   were favored under acidic conditions, as they could deactivate the iron ions at pH >5.0

268   (Zhong et al., 2019). Thus, the enhanced removal at the acidic pH was attributed to the

269   Fenton-like degradation. Fe^0-BC and Fe_3C-AB exhibited diverse removal performances

270   at different initial pH values, indicating that different removal mechanisms were

271   involved. The optimal pH was observed at pH 8.0, and the removal was lower under

272   acidic (pH 5.0) or strongly alkaline (pH 11.0) conditions. The point of zero charge

273   (pH_{PZC}) of Fe^0-BC and Fe_3C-AB was determined to be 5.25 and 5.21, respectively.

274   Given that BPA is electro-positive at pH <9.0, the electrostatic repulsion reduced the

275   removal at pH 5.0. In contrast, at pH 8.0, the O-containing groups on the Fe/C

276   composites were fully ionized (–O⁻, –COO⁻), resulting in electrostatic attraction

277   interactions and hydrogen bonding (Quan et al., 2019). Furthermore, based on the pK_a

278   value of BPA that ranged from 9.6 to 10.2, BPA was electro-negative at pH 11.0 (BPA^{2-}

279   and $HBPA^-$) (Yoon et al., 2003). The Fe_3C-AB composite was also negatively charged

280   at pH 11.0, and the electrostatic repulsion was further enhanced, reducing the BPA

281   removal. However, the decrease in BPA removal was only 24.3%, indicating that

282   Fe_3C-AB can perform well over a wide pH range.

283   *3.3.3. Ionic strength*

284   Inorganic salts, such as NaCl, are widely present in various concentrations in real

285   wastewater samples. It was reported that the Cl^- in the groundwater of Yuncheng Basin,

286   China was 1686 mg/L and tannery industrial waste water contained high up to 80 g/L of

287   NaCl (Lefebvre and Moletta, 2006; Li et al., 2016). The existence of NaCl could either

288   improve or impair organic contaminant removal (Li et al., 2020; Yang et al., 2018). Fig.

289   4c shows the effect of ionic strength on BPA removal. The presence of NaCl increased

290   the removal efficiency of BPA on Fe^0 and Fe_3C. We assumed that $^{\bullet}Cl$ might produce

291 (Fang et al., 2014) and consequently enhanced BPA decomposition (Eqs. 9-10).

292 However, Fe/C composites behaved differently in the presence of NaCl. Specifically,

293 the BPA removal efficiency reduced by 42.4% and 14.6% in the presence of 50 mg/L

294 NaCl for Fe^0-BC and Fe_3C-AB, respectively, likely because of the occupation of the

295 active adsorption sites of biochars. Nevertheless, although the removal efficiency

296 decreased with increasing NaCl concentrations, the removal capacity of Fe_3C-AB

297 remained about 3 times higher than that of Fe^0-BC.

298 $$^\bullet OH + Cl^- \rightarrow {}^\bullet ClOH^- \qquad (9)$$

299 $$^\bullet ClOH^- + H^+ \rightarrow {}^\bullet Cl + H_2O \qquad (10)$$

300 *3.3.4. Different kind of waters*

301 In order to evaluate the BPA removal performance from different kind of waters

302 using the prepared Fe/C composites, three different water substrates were tested (Table

303 S4). Fig. 4d shows that the BPA removal performance in the tap water and lake water

304 reduced significantly in Fe_3C, Fe^0-BC and Fe_3C-AB systems and the lake water had a

305 stronger impact than the tap water. These decreases were caused by the competitive

306 Fenton oxidation of natural organic matter (Jiang et al., 2018). The inhibitive effect was

307 negligible for Fe^0 in tap water and a small reduction was happened in lake water due to

308 the higher content of total organic carbon (5.68 mg/L). However, despite the removal of

309 BPA which reduced by 35.9% for Fe_3C-AB, its overall removal efficiency was still 3

310 times higher than that of Fe^0-BC.

311 *3.4. Removal mechanisms*

312 *3.4.1. Adsorption mechanism*

313 The adsorption mechanism of BPA on the Fe/C composites was studied via XPS

314 (Figs. S7a-7d), where the wide O_{1s} peaks suggested the presence of different chemical

315 oxygen states including the organic oxygen atoms of carboxyl, carbonyl, alkoxyl, and

13

ether groups, and the inorganic oxygen atoms of iron oxides (Datsyuk et al., 2008). The binding energies of 530.1–530.4, 531.4–531.6, and 532.2–533.4 eV in the O_{1s} region were attributed to the O–Fe, O=C–OH, and O–C bonds, respectively (Hu et al., 2015; Oh et al., 2014). All peaks shifted significantly after BPA adsorption, indicating that the O-containing functional groups of the Fe/C composites were involved in BPA removal. In particular, the adsorption of BPA on Fe^0-BC reduced the amount of O–C groups, indicating their involvement in the removal process as adsorption sites. Unlike Fe^0-BC, the O=C–OH group was mainly responsible for BPA adsorption on Fe_3C-AB. Previous studies have reported that the O=C–OH group could form a hydrogen bond with BPA (Quan et al., 2019; Zhang et al., 2014). Thus, DFT calculations were performed to confirm the formation of hydrogen bonds. Benzoic acid, whose carboxylic group is ionized at pH 8.0, was used as a model of the carboxylic group in the Fe/C composites to interact with the BPA molecule. The results in Figs. S7e-7f display that BPA was bound to the carboxylic group through a hydrogen bond with interaction energies of −7.72 and −7.80 kcal/mol. The negative energy values suggested that the carboxylic group spontaneously interacted with the BPA hydroxyl group via a hydrogen bond. Consequently, the synergistic functions of the hydrogen bonds and the pore filling may increase BPA removal capacity with a faster removal rate by Fe_3C-AB as compared to Fe^0-BC.

3.4.2. Reactive oxygen species responsible for degradation

Fig. 5a shows the BPA removal efficiency in the presence of 0.1 M *tert* butyl alcohol, 1 mM benzoquinone, and 60 mg/L β-carotene for Fe_3C-AB, was decreased from 32.7% to 31%, 29.4%, and 20.6%, respectively. Hence, $^1O_2$ was identified as the most important ROS (Fig. 5b), as the BPA degradation efficiency induced by $^1O_2$ was considerably high (37.0%). Moreover, ~52.3% of the BPA removal efficiency for

341   Fe$_3$C-AB was due to the degradation mechanism, which was higher than the total

342   removal of BPA by Fe^0-BC (15.4%). In the Fe^0-BC system, ~83.6% of the BPA removal

343   was caused by degradation.

344   Electron spin resonance (ESR) measurements were also performed to detect the

345   ROS species during BPA removal. Based on Figs. 5c–5d, the characteristic peaks of

346    $^•$OH and $^•$O$_2^-$ with signal intensity ratios of 1:2:2:1 and 1:1:1:1 were obtained in water

347   and methanol, respectively. The typical three-line ESR spectra were also obtained (Fig.

348   5e), confirming the presence of ^{1}O$_2$ in the Fe/C systems. All these findings indicated

349   that the $^•$OH, $^•$O$_2^-$, and ^{1}O$_2$ species played a significant role in BPA degradation.

350   Moreover, the signal intensity of $^•$OH was greater in Fe^0-BC. However, the signal

351   intensity of $^•$O$_2^-$ and ^{1}O$_2$ were higher in the Fe$_3$C-AB system than in Fe^0-BC, indicating

352   that Fe$_3$C-AB could enhance $^•$O$_2^-$ and ^{1}O$_2$ generation due to the well-dispersed Fe$_3$C

353   nanoparticles in biochar.

354   Eqs. 11-16 illustrate the reactions in Fe^0-BC and Fe$_3$C-AB systems (Bao et al.,

355   2020; Cuervo Lumbaque et al., 2019; Yang et al., 2018). The generation of ROS by

356   Fe^0-BC and Fe$_3$C-AB was initiated through the oxidation of Fe^0 by dissolved oxygen to

357   form H$_2$O$_2$ (Eq.11) and the decomposition of H$_2$O$_2$ could produce $^•$OH (Eq.12). The

358   concentrations of *in situ* formed H$_2$O$_2$ were 97.6 µM and 72.5 µM when Fe^0-BC and

359   Fe$_3$C-AB reacted with H$_2$O for 24 h, respectively. Further, they were observed to

360   decrease after BPA addition, indicating the decomposition of H$_2$O$_2$ by Fe/C composites

361   exhibited potential for BPA degradation due to the generation of $^•$OH (Fig. S8). The

362   oxidation of Fe^{2+} which derived from the corrosion of Fe^0 under the anaerobic condition

363   could also generate $^•$OH (Eq.13). Meanwhile, the surface-adsorbed water could donate

364   an electron to Fe^{3+} to engender $^•$OH (Wang et al., 2021). After purging N$_2$, the removal

365   efficiency of BPA was decreased (Fig. S9), indicating that $^•$O$_2^-$ was produced via

366 electron transfer from Fe^{2+} to O_2 (Eq.14), while recombination of the $^{\cdot}O_2^{-}$ species and

367 the reaction between $^{\cdot}O_2^{-}$ and $^{\cdot}OH$ afforded $^1O_2$ (Eqs.15-16) (Xi et al., 2021). H_3PO_4

368 activation was reported to increase the number of electron transferred per O_2 molecule

369 (Puziy et al., 2020) and the greatest improvement in oxygen reduction reaction activity

370 was observed for P/Fe ratios of 0.33 (The P/Fe ratio in this paper was 0.30). The

371 electron transfer processes could also be facilitated by graphitized carbon of Fe_3C-AB to

372 activate O_2 to generate more $^{\cdot}O_2^{-}$ and $^1O_2$.

373
$$Fe^0 + O_2 + 2H^+ \rightarrow Fe^{2+} + H_2O_2 \tag{11}$$

374
$$Fe^0 + 2H_2O_2 \rightarrow Fe^{2+} + 2^{\cdot}OH + 2OH^- \tag{12}$$

375
$$Fe^{2+} + H_2O_2 \rightarrow Fe^{3+} + ^{\cdot}OH + OH^- \tag{13}$$

376
$$Fe^{2+} + O_2 \rightarrow Fe^{3+} + ^{\cdot}O_2^{-} \tag{14}$$

377
$$^{\cdot}O_2^{-} + ^{\cdot}O_2^{-} + 2H^+ \rightarrow {}^1O_2 + H_2O_2 \tag{15}$$

378
$$^{\cdot}O_2^{-} + ^{\cdot}OH \rightarrow {}^1O_2 + OH^- \tag{16}$$

379 Fig. 6 summarizes the possible mechanisms governing BPA removal by Fe/C

380 composites. BPA was quickly adsorbed by the abundant pores in Fe_3C-AB, and the

381 greater pore volume and the formation of hydrogen bonds enhanced the adsorption

382 capacity of BPA on Fe_3C-AB. In addition, the degradation and adsorption occurred

383 simultaneously in both Fe/C systems. In Fe^0-BC and Fe_3C-AB, $^{\cdot}OH$, $^{\cdot}O_2^{-}$, and $^1O_2$ were

384 mainly produced and the generation of $^1O_2$ was predominantly favored in Fe_3C-AB. The

385 graphitized carbon used as the electron donor in Fe_3C-AB could provide more electrons

386 to O_2 for generating $^1O_2$. Thus, the Fe_3C-loaded activated biochar was beneficial to $^1O_2$

387 generation.

388 *3.4.3. Degradation pathways*

389 Figs. 7, S11-13 showed the high-performance liquid chromatography with mass

390 spectra of the reaction products after 50 min, 150 min and 24 h. Additional peak

corresponding to by-product was detected at 50 min, indicating the degradation of BPA was happened (Fig. S11). In the case of Fe^0-BC, most BPA molecules (*m/z* 227, retention time (RT): 4.99 min) were not completely adsorbed or degraded at 24 h. Six main by-products were identified in this system, among which the peak intensity of product J (propanedioic acid, *m/z* 103, RT: 1.08 min) was the highest. In the Fe$_3$C-AB system, most BPA molecules were adsorbed or degraded into other by-products. In particular, ten by-products were detected with relatively low peak intensities, implying that Fe$_3$C-AB had both strong adsorption and degradation capacities.

The degradation pathways of BPA by Fe/C composites were thus proposed, consisting of two different routes (Figs. 7c-7d). In route 1 of Fe^0-BC (Fig. 7c), the two methylene groups of BPA were cleaved and the demethylated product A was formed (*m/z* 199, RT: 1.96 min). Then, isomerization, ring-closing, and oxidation reactions followed, which afforded intermediate C (*m/z* 185, RT: 1.58 min). Alternatively, in route 2, BPA was first oxidized to product B (*m/z* 191, RT: 3.22 min) through a ring-closing reaction. Afterward, products C and H (*m/z* 149, RT: 4.35 min) were further oxidized to benzoic acid (product I, *m/z* 121, RT: 3.07 min). Propanedioic acid, with the lowest molecular weight (product J), was the final degradation product of both routes using Fe^0-BC. In contrast, the degradation mediated by the Fe$_3$C-AB system was more complex. In route 1, the ring-closing and oxidation reactions of product C led to the formation of product D (*m/z* 183, RT: 2.98 min), which was subsequently oxidized to 6-hydroxymethyl-2-naphthol (product E, *m/z* 173, RT: 0.99 min). In route 2, product B was oxidized to product F (*m/z* 165, RT: 1.83 min), then dehydrogenation process induced the formation of G (*m/z* 163, RT: 3.54 min). The loss of methyl group accounted for the production of H. At last, product I was transformed into butenedioic acid (J, *m/z* 115, RT: 4.14 min). The degradation products of D, E, F and G in Fe^0-BC

416   system were not detected which might be adsorbed on Fe^0-BC material.

417   Further, density functional reactivity theory (DFRT) was used to analyze the ROS

418   attack site and Fenton reactivity. In the Fukui function, $f^-(r)$ and $f^0(r)$ could be used to

419   indicate the difficulty of a molecule to being attacked by electrophilic reagents and free

420   radicals, and the larger the value, the more vulnerable a molecule would be attacked by

421   electrophilic reagents and free radicals (Cao et al., 2015). The dual descriptor $\Delta f(r)$

422   could also describe the site where the molecule was susceptible to electrophilic attack,

423   and the more negative the area, the more susceptible to electrophilic attack (Morell et al.,

424   2005). The ROS were electrophiles, hence, $f^-(r)$, $f^0(r)$ and $\Delta f(r)$ were used to predict the

425   site of BPA being attacked by ROS. The isosurface distribution of $f^-(r)$, $f^0(r)$ and $\Delta f(r)$

426   was shown in Fig. S14. The green and blue parts denoted the positive and negative

427   values, respectively. The positive parts (green) of $f^0(r)$ and $f^-(r)$ were vulnerable to free

428   radicals and electrophilic attacks, and the negative parts (blue) of $\Delta f(r)$ were vulnerable

429   to electrophilic attacks. According to $f^0(r)$ and $f^-(r)$, the attack area of ROS mainly

430   occurred in the benzene ring, C13 and C15, however, the attack activity of each site by

431   ROS was different. Furthermore, according to $\Delta f(r)$, the attack area of ROS was more

432   biased toward the C3, C6, C9, C12, C13, C15, O1, and O2 regions.

433   To further understand the reactivity of each atom attacked by ROS, the condensed

434   Fukui function values (f_A^- and f_A^0) and the condensed dual descriptor (Δf_A) of each atom

435   were calculated (Fig. 8, Table S5). ROS would preferentially attack atoms with larger

436   f_A^- and f_A^0 values and more negative Δf_A values (Yin et al., 2019). For the alkyl chain

437   (C13-C14-C15), C13 and C15 both have the largest f_A^0 and f_A^- values (Figs. 8a and 8b),

438   and the Δf_A value was negative (Fig. 8c), hence, ROS would preferentially attack C13

439   and C15 on the alkyl chain, which corresponded to the products of degradation pathway

440   1.

441   For the benzene ring, C5 and C8 have the largest f_A^0 values (Fig. 8a, Table S5), and

442 ROS as a free radical will attack the C5 and C8 sites preferentially. Among the benzene

443 ring and its connecting atoms, O1, C3, C5, and C9 and its central symmetry atoms O2,

444 C12, C8, and C9 have larger f_A^- values, but only O1, C3, and C6 and its central

445 symmetry atoms O2, C12, and C9 showed negative Δf_A values (Fig. 8c), indicating that

446 ROS as an electrophile will preferentially attack O1, C3, and C6 and their centrally

447 symmetric atoms. The values of the condensed Fukui functions and condensed dual

448 descriptors of centrally symmetric atoms were not equal (Table S5). Notably, ring I had

449 larger f_A^0 and f_A^- values than ring II (Figs. 8d and 8e). At the same time, ring I had a

450 smaller Δf_A value than ring II. This indicated that the attack of ROS on rings I and II

451 was asymmetric, ROS would preferentially attack ring I, which corresponded to the

452 product of degradation pathway 2.

4. Conclusions

454   Porous Fe_3C-AB was successfully synthesized through a facile route of pyrolyzing

455 H_3PO_4 pre-treated biochar with $Fe(NO_3)_3$ at 600 °C to efficiently remove BPA from

456 contaminated aqueous solution. The high removal rate and capacity of Fe_3C-AB for

457 BPA were mainly attributed to its improved surface area and porous structure compared

458 to that of Fe^0-BC. The excellent performance of Fe_3C-AB was maintained even under

459 extreme conditions, such as high salinity, different water sources, and a wide pH range

460 from 5.0 to 11.0. In addition, we confirmed that both adsorption and degradation

461 mechanisms were involved in BPA removal by Fe/C composites. The development of

462 hydrogen bonds and the microporous structure of Fe_3C-AB resulted in its high

463 adsorption capacity. Nevertheless, Fe_3C-AB also exhibited oxidative activity and $^\bullet OH$,

464 $^\bullet O_2^-$, and $^1O_2$ were generated for BPA degradation. Quenching experiments provided

465 evidence that $^1O_2$ accounted for 37.0% in the removal of BPA by Fe_3C-AB. DFRT

calculation showed that ROS would preferentially attack ring I, which corresponded to the product of degradation pathway 2. Given the favorable stability, remarkable adsorption capacity, oxidative characteristics, excellent reusability, higher PC, and lower cost of Fe_3C-AB, compared to other materials and Fe/C composites, this novel Fe_3C-modified biochar with multiple applications could promote the elimination of other organic contaminants over a wide pH range and increase the resistance towards NaCl. The mechanisms for the *in situ* adsorption and oxidation degradation would provide a theoretical basis for the application of this system without purging O_2 or adding extra H_2O_2 in the treatment of organic contaminants in water and create economic values.

Declaration of Competing Interest

The authors declare that they have no known competing financial interests or personal relationships that could have appeared to influence the work reported in this paper.

Appendix A. Supplementary data

Supplementary data to this article can be found in supplementary information.

References

Acosta, R., Nabarlatz, D., Sánchez-Sánchez, A., Jagiello, J., Gadonneix, P., Celzard, A., Fierro, V., 2018. Adsorption of Bisphenol A on KOH-activated tyre pyrolysis char, J. Environ. Chem. Eng. 6, 823-833.

491 Ahmed, M.B., Zhou, J.L., Ngo, H.H., Guo, W.S., Johir, M.A.H., Sornalingam, K.,

492 Belhaj, D., Kallel, M., 2017. Nano-Fe^0 immobilized onto functionalized biochar gaining

493 excellent stability during sorption and reduction of chloramphenicol via transforming to

494 reusable magnetic composite. Chem. Eng. J. 322, 571-581.

495 Bao, T., Damtie, M.M., Hosseinzadeh, A., Wei, W., Jin, J., Phong Vo, H.N., Ye, J.S., Liu,

496 Y., Wang, X.F., Yu, Z.M., Chen, Z.J., Wu, K., Frost, R.L., Ni, B.J., 2020.

497 Bentonite-supported nano zero-valent iron composite as a green catalyst for bisphenol A

498 degradation: Preparation, performance, and mechanism of action. J. Environ. Manage.

499 260, 110105.

500 Belfroid, A., van Velzen M., van der Horst, B., Vethaak, D., 2002. Occurrence of

501 bisphenol A in surface water and uptake in fish evaluation of field measurements.

502 Chemosphere 49, 97-103.

503 Cao, J., Ren, Q., Chen, F., Lu, T., 2015. Comparative study on the methods for

504 predicting the reactive site of nucleophilic reaction. Sci. China Chem. 58(12),

505 1845-1852.

506 Chen, T., Ling, L., Deng, S., Shi, G., Zhang, S., Zhang, Y., Deng, O., Wang, L., Zhang J.,

507 Wei, L., 2018. Sorption of tetracycline on H_3PO_4 modified biochar derived from rice

508 straw and swine manure. Bioresour. Technol. 267, 431-437.

509 Cuervo Lumbaque, E., Lopes Tiburtius, E.R., Barreto-Rodrigues, M., Sirtori, C., 2019.

510 Current trends in the use of zero-valent iron (Fe^0) for degradation of pharmaceuticals

511 present in different water matrices. Trends Environ. Anal. Chem. 24, e00069.

512 Datsyuk, V., Kalyva, M., Papagelis, K., Parthenios, J., Tasis, D., Siokou, A., Kallitsis, I.,

513 Galiotis, C., 2008. Chemical oxidation of multiwalled carbon nanotubes. Carbon 46,

514 833-840.

515 Devi, P., Saroha, A.K., 2014. Synthesis of the magnetic biochar composites for use as an

516 adsorbent for the removal of pentachlorophenol from the effluent. Bioresour. Technol.

517 169, 525-531.

518 European Food Safety Authority, 2016. Bisphenol A (BPA) hazard assessment protocol.

519 EFSA J.

520 Fang, J., Fu, Y., Shang, C., 2014. The roles of reactive species in micropollutant

521 degradation in the UV/free chlorine system. Environ. Sci. Technol. 48, 1859-1868.

522 Fierro, V., Torné-Fernández, V., Celzard, A., 2006. Kraft lignin as a precursor for

523 microporous activated carbons prepared by impregnation with ortho-phosphoric acid:

524 Synthesis and textural characterisation, Micropor. Mesopor. Mat. 92, 243-250.

525 Guediri, A., Bouguettoucha, A., Chebli, D., Chafai, N., Amrane, A., 2020. Molecular

526 dynamic simulation and DFT computational studies on the adsorption performances of

527 methylene blue in aqueous solutions by orange peel-modified phosphoric acid. J. Mol.

528 Struct. 1202, 127290.

529 Hu, X., Ding, Z.H., Zimmerman, A.R., Wang, S.S., Gao, B., 2015. Batch and column

530 sorption of arsenic onto iron-impregnated biochar synthesized through hydrolysis.

531 Water Res. 68, 206-216.

532 Jiang, W.L., Xia, X., Han, J.L., Ding, Y.C., Haider, M.R., Wang, A.J., 2018. Graphene

533 modified electro-Fenton catalytic membrane for in situ degradation of antibiotic

534 florfenicol. Environ. Sci. Technol. 52, 9972-9982.

535 Kruk, M., Jaroniec, M., 2001. Gas adsorption characterization of ordered

536 organic-inorganic nanocomposite materials. Chem. Mater. 13, 3169-3183.

537 Kumar, M., Xiong, X., Sun, Y., Yu, I.K.M., Tsang, D.C.W., Hou, D., Gupta, J., Bhaskar,

538 T., Pandey, A., 2020. Critical review on biochar-supported catalysts for pollutant

539 degradation and sustainable biorefinery. Adv. Sustainable Syst. 1900149.

540 Lefebvre, O., Moletta, R., 2006. Treatment of organic pollution in industrial saline

wastewater: A literature review. Water Res. 40(20), 3671-3682.

Li, C.C., Liu, T., Xu, S., Gao, X.B., Wang, Y.X., 2016. Groundwater salinization in shallow aquifers adjacent to a low-altitude inland salt lake: a case study at Yuncheng Basin, northern China. Environ. Earth Sci. 75, 370.

Li, D.H., Sun, Y.Y., Chen, S., Yao, J.Y., Zhang, Y.H., Xia, Y.Z., Yang, D.J., 2018. Highly porous FeS/carbon fibers derived from Fe-Carrageenan biomass: High-capacity and durable anodes for sodium-ion batteries. ACS Appl. Mater. Inter. 10, 17175-17182.

Li, J.F., Lan, H.C., Liu, H.J., Zhang, G., An, X.Q., Liu, R.P., Qu, J.H., 2019. Intercalation of nanosized Fe_3C in iron/carbon to construct multifunctional interface with reduction, catalysis, corrosion resistance, and immobilization capabilities, ACS Appl. Mater. Interf. 11, 15709-15717.

Li, Z., Sun, Y.Q., Yang, Y., Han, Y.T., Wang, T.S., Chen, J.W., Tsang, D.C.W., 2020. Biochar-supported nanoscale zero-valent iron as an efficient catalyst for organic degradation in groundwater, J. Hazard. Mater. 383, 121240.

Liang, L.P., Xue, Y.Y., Tian, G.L., Mao, Q.L., Lou, Z.X., Wu, Q., Wang, Q., Du, J.S., Meng, X., 2019. Performance of selenate removal by biochar embedded nano zero-valent iron and the biological toxicity to *Escherichia coli*. Rsc. Adv. 9(45), 26136-26141.

Lu, T., Chen, F., 2012. Multiwfn: a multifunctional wavefunction analyzer. J. Comput. Chem. 33(5), 580-592.

Mohan, D., Pittman, C.U., 2006. Activated carbons and low cost adsorbents for remediation of tri- and hexavalent chromium from water. J. Hazard. Mater. 137(2), 762-811.

Morell, C., Grand, A., Toro-Labbé, A., 2005. New dual descriptor for chemical reactivity. J. Phys. Chem. A 109, 205-212.

Neeli, S.T., Ramsurn, H., 2018. Synthesis and formation mechanism of iron nanoparticles in graphitized carbon matrices using biochar from biomass model compounds as a support. Carbon 134, 480-490.

Newcombe, G., Drikas, M., 1997. Adsorption of NOM onto activated carbon: Electrostatic and non-electrostatic effects. Carbon 35, 1239-1250.

Oh, Y.J., Yoo, J.J., Kim, Y.I., Yoon, J.K., Yoon, H.N., Kim, J.H., Park, S.B., 2014. Oxygen functional groups and electrochemical capacitive behavior of incompletely reduced graphene oxides as a thin-film electrode of supercapacitor. Electrochimica Acta 116, 118-128.

Pang, Y.X., Ruan, Y., Feng, Y., Diao, Z.H., Shih, K.M., Hou, L.A., Chen, D.Y., Kong, L.J., 2019. Ultrasound assisted zero valent iron corrosion for peroxymonosulfate activation for Rhodamine-B degradation, Chemosphere 228, 412-417.

Prahas, D., Kartika, Y., Indraswati, N., Ismadji, S., 2008. Activated carbon from jackfruit peel waste by H_3PO_4 chemical activation: Pore structure and surface chemistry characterization. Chem. Eng. J. 140, 32-42.

Puziy, A.M., Poddubnaya, O.I., Gawdzik, B., Tascón, J.M.D., 2020. Phosphorus-containing carbons: Preparation, properties and utilization. Carbon 157, 796-846.

Qian, L., Chen, Y., Ouyang, D., Zhang, W., Han, L., Yan, J., Kvapil, P., Chen, M., 2020. Field demonstration of enhanced removal of chlorinated solvents in groundwater using biochar-supported nanoscale zero-valent iron. Sci. Total Environ. 698, 134215.

Qin, F.X., Jia, S.Y., Liu, Y., Li, H.Y., Wu, S.H., 2015. Adsorptive removal of bisphenol A from aqueous solution using metal-organic frameworks. Desalin. Water Treat. 54, 93-102.

Quan, L.D., Dang, N.H., Tu, T.H., Linh, V.N.P., Thy, L.T.M., Nam, H.M., Phong, M.T.,

Hieu, N.H., 2019. Preparation of magnetic iron oxide/graphene aerogel nanocomposites for removal of bisphenol A from water. Synthetic Met. 255, 116106.

Sun, Y.Q., Yu, I.K.M., Tsang, D.C.W., Cao, X.D., Lin, D.H., Wang, L.L., Graham, N.J.D., Alessi, D.S., Komarek, M., Ok, Y.S., Feng, Y.J., Li, X.D., 2019. Multifunctional iron-biochar composites for the removal of potentially toxic elements, inherent cations, and hetero-chloride from hydraulic fracturing wastewater. Environ. Int. 124, 521-532.

vom Saal, F.S., Hughes, C., 2005. An extensive new literature concerning low-dose effects of bisphenol A shows the need for a new risk assessment. Environ. Health Persp. 113, 926-933.

Tammam, R.H., Touny, A.H., Abdesalam, M.E., Saleh, M.M., 2018. Mesoporous NiPh/carbon fibers nanocomposite for enhanced electrocatalytic oxidation of ethanol, J. Electroanal Chem. 823, 128-136.

Wan, Z., Sun, Y., Tsang, D. C., Xu, Z., Khan, E., Liu, S. H., Cao, X., 2020. Sustainable impact of tartaric acid as electron shuttle on hierarchical iron-incorporated biochar. Chem. Eng. J. 395, 125138.

Wang, G.X., Yang, J., Park, J., Gou, X.L., Wang, B., Liu, H., Yao, J., 2008. Facile synthesis and characterization of graphene nanosheets. J. Phys. Chem. C 112, 8192-8195.

Wang, H.Z., Guo, W.Q., Liu, B.H., Wu, Q.L., Luo, H.C., Zhao, Q., Si, Q.S., Sseguya, F., Ren, N.Q., 2019. Edge-nitrogenated biochar for efficient peroxydisulfate activation: An electron transfer mechanism. Water Res. 160, 405-414.

Wang, Y., Lyu, L., Wang, D., Yu, H.Q., Li, T., Gao, Y., Li, F. Crittenden, J.C., Zhang, L.L., Hu, C., 2021. Cation–π induced surface cleavage of organic pollutants with $^{\bullet}$OH formation from H_2O for water treatment. iScience, 24, 102874.

Shih, Y.H., Chen, M.Y., Su, Y.F., Tso, C.P., 2016. Concurrent oxidation and reduction of

pentachlorophenol by bimetallic zerovalent Pd/Fe nanoparticles in an oxic water. J. Hazard. Mater. 301, 416-423.

Xi, T., Li, X., Zhang, Q., Liu, N., Niu, S., Dong, Z.J., Lyu., C., 2021. Enhanced catalytic oxidation of 2,4-dichlorophenol via singlet oxygen dominated peroxymonosulfate activation on CoOOH@Bi$_2$O$_3$ composite. Front. Environ. Sci. Eng. 2021, 15(4), 55.

Yan, Q.G., Wan, C.X., Liu, J., Gao, J.S., Yu, F., Zhang, J.L., Cai, Z.Y., 2013. Iron nanoparticles in situ encapsulated in biochar-based carbon as an effective catalyst for the conversion of biomass-derived syngas to liquid hydrocarbons. Green Chem. 15, 1631-1640.

Yang, F., Zhang, S.S., Sun, Y.Q., Du, Q., Song, J.P., Tsang, D.C.W., 2019. A novel electrochemical modification combined with one-step pyrolysis for preparation of sustainable thorn-like iron-based biochar composites, Bioresour. Technol. 274, 379-385.

Yang, S.S., Wu, P.X., Liu, J.Q., Chen, M.Q., Ahmed, Z., Zhu, N.W., 2018. Efficient removal of bisphenol A by superoxide radical and singlet oxygen generated from peroxymonosulfate activated with Fe^0-montmorillonite. Chem. Eng. J. 350, 484-495.

Yao, L., Yang, J.J., Zhang, P.X., Deng, L.B., 2018. In situ surface decoration of Fe$_3$C/Fe$_3$O$_4$/C nanosheets: Towards bi-functional activated carbons with supercapacitance and efficient dye adsorption, Bioresour. Technol. 256, 208-215.

Yin, R., Guo, W., Wang, H., Du, J., Wu, Q., Chang, J.S., Ren, N., 2019. Singlet oxygen-dominated peroxydisulfate activation by sludge-derived biochar for sulfamethoxazole degradation through a nonradical oxidation pathway: Performance and mechanism. Chem. Eng. J. 357, 589-599.

Yoon, Y.M., Westerhoff, P., Snyder, S.A., Esparza, M., 2003. HPLC-fluorescence detection and adsorption of bisphenol A, 17 beta-estradiol, and 17 alpha-ethynyl estradiol on powdered activated carbon. Water Res. 37, 3530-3537.

641 Zeng, S.Q., Choi, Y.K., Kan, E.S., 2021. Iron-activated bermudagrass-derived biochar

642 for adsorption of aqueous sulfamethoxazole: Effects of iron impregnation ratio on

643 biochar properties, adsorption, and regeneration. Sci. Total Environ. 750, 141691.

644 Zhang, H.M., Ruan, Y., Liang, A.P., Shih, K.M., Diao, Z.H., Su, M.H., Hou, L.A., Chen,

645 D.Y., Lu, H., Kong, L.J., 2019. Carbothermal reduction for preparing nZVI/BC to

646 extract uranium: Insight into the iron species dependent uranium adsorption behavior. J.

647 Clean. Prod. 239, 117873.

648 Zhang, Z.H., Chen, X., Rao, W., Chen, H.J., Cai, R., 2014. Synthesis and properties of

649 magnetic molecularly imprinted polymers based on multiwalled carbon nanotubes for

650 magnetic extraction of bisphenol A from water. J. Chromatogr. B 965, 190-196.

651 Zhao, N., Zhao, C.F., Lv, Y.Z., Zhang, W.F., Du, Y.G., Hao, Z.P., Zhang, J., 2017.

652 Adsorption and coadsorption mechanisms of Cr(VI) and organic contaminants on

653 H_3PO_4 treated biochar. Chemosphere 186, 422-429.

654 Zhao, N., Yin, Z., Liu, F., Zhang, M.Y., Lv, Y.Z., Hao, Z.P., Pan, G., Zhang, J., 2018.

655 Environmentally persistent free radicals mediated removal of Cr(VI) from highly saline

656 water by corn straw biochars. Bioresour. Technol. 260, 294-301.

657 Zhao, N., Liu, K.Y., He, C., Gao, J., Zhang, W.H., Zhao, T.J., Tsang, D.C.W., Qiu, R.L.,

658 2020. Singlet oxygen mediated the selective removal of oxytetracycline in C/Fe$_3$C/ Fe^0

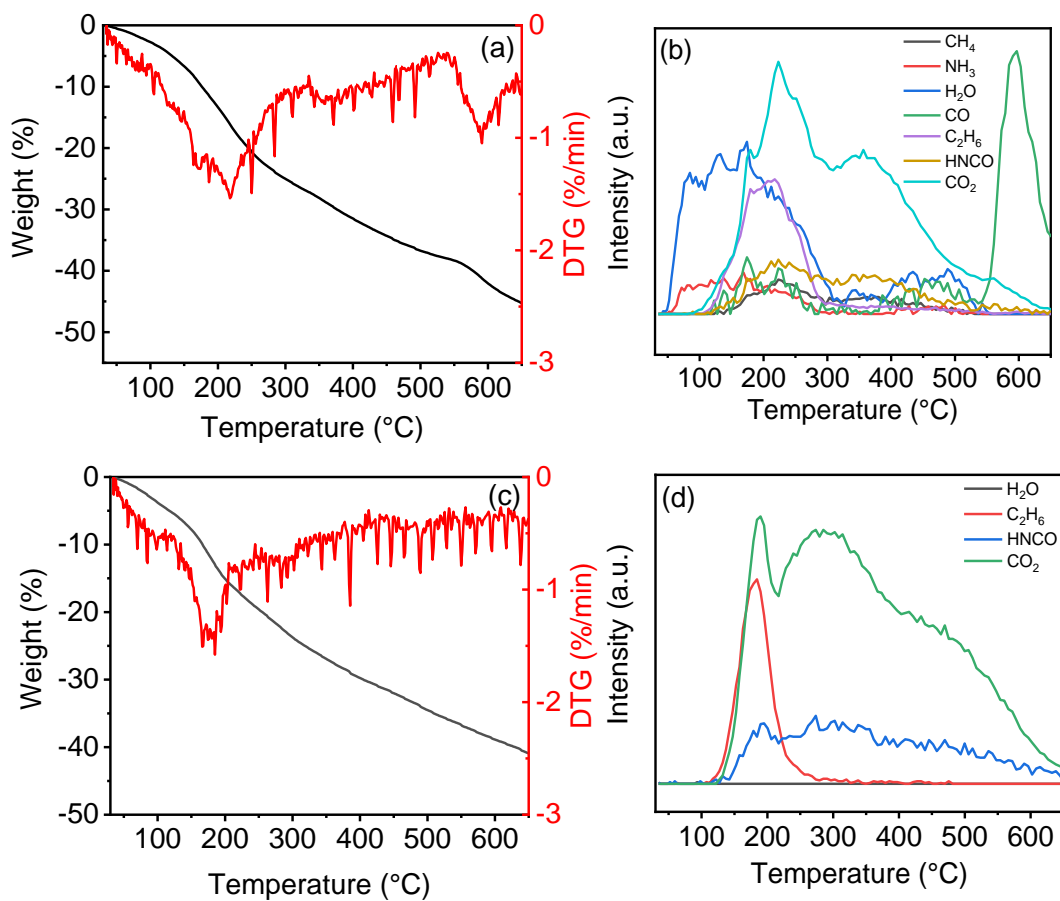659 system as compared to chloramphenicol. Environ. Int. 143, 105899.

660 Zhao, N., Zhao, C.F., Tsang, D.C.W., Liu, K.Y., Zhu, L., Zhang, W.H., Zhang, J., Tang,

661 Y.T., Qiu, R.L., 2021. Microscopic mechanism about the selective adsorption of Cr(VI)

662 from salt solution on O-rich and N-rich biochars. J. Hazard. Mater. 404, 124162.

663 Zhong, P., Yu, Q., Zhao, J., Xu, S., Qiu, X., Chen, J., 2019. Degradation of bisphenol A

664 by Fe-Al layered double hydroxides: A new synergy of homo- and heterogeneous

665 Fenton systems. J. Colloid Interf. Sci. 552, 122-133.

666   Zhu, S., Jin, C., Duan, X., Wang, S., Ho, S. H., 2020. Nonradical oxidation in persulfate

667   activation by graphene-like nanosheets (GNS): Differentiating the contributions of

668   singlet oxygen ($^1O_2$) and sorption-dependent electron transfer. Chem. Eng. J. 393,

669   124725.

670

671
672
673
674
675
676
677
678
679
680
681
682
683
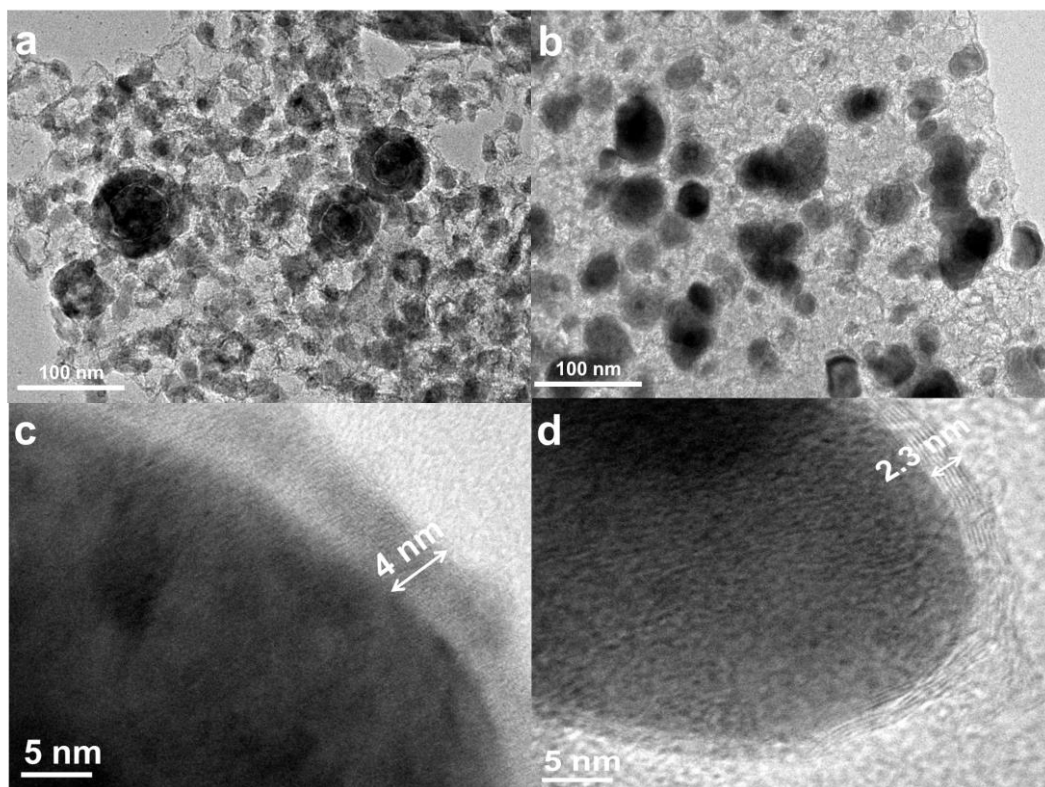
684   **Fig. 1.** TEM images of (a) Fe^0-BC, (b) Fe$_3$C-AB, and the single iron sphere of (c) Fe^0-BC,

685   (d) Fe$_3$C-AB.

686

687

Fig. 2. Analysis of the outlet gases from the decomposition of the precursors for (a, b) Fe^0-BC and (c, d) Fe_3C-AB by TG-MS.
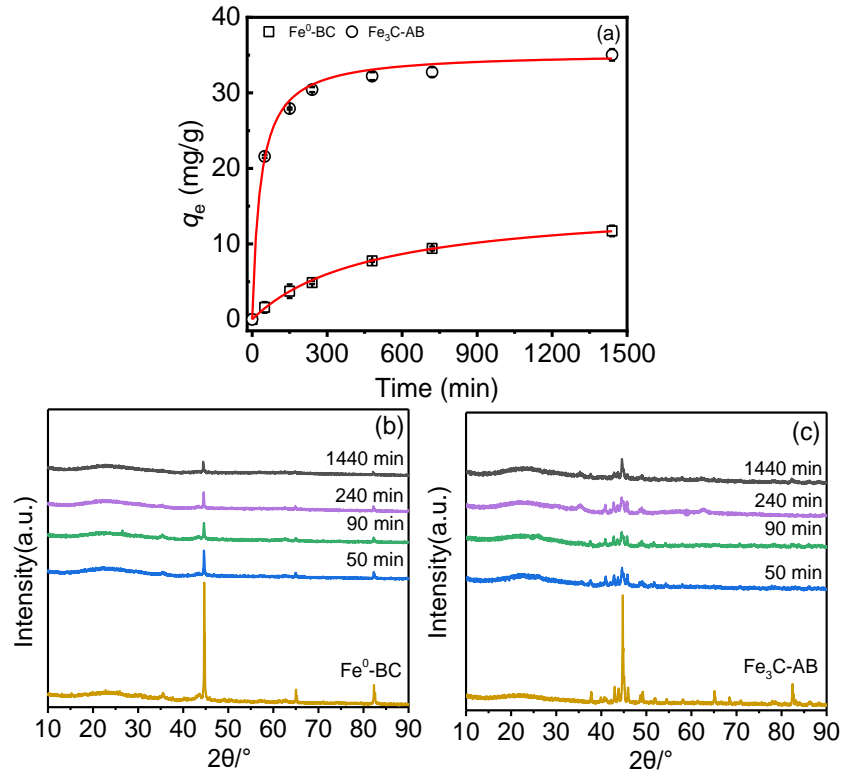
Fig. 3. (a) The removal kinetics of BPA. Lines represent pseudo second-order kinetic fitting and the bars are standard deviation. All samples were run in duplicate. The experiment conditions were 50 mg/L initial concentration at pH 8, 25°C from high purity water. XRD patterns of (b) Fe⁰-BC, and (c) Fe₃C-AB after reacting with BPA at 24 h.
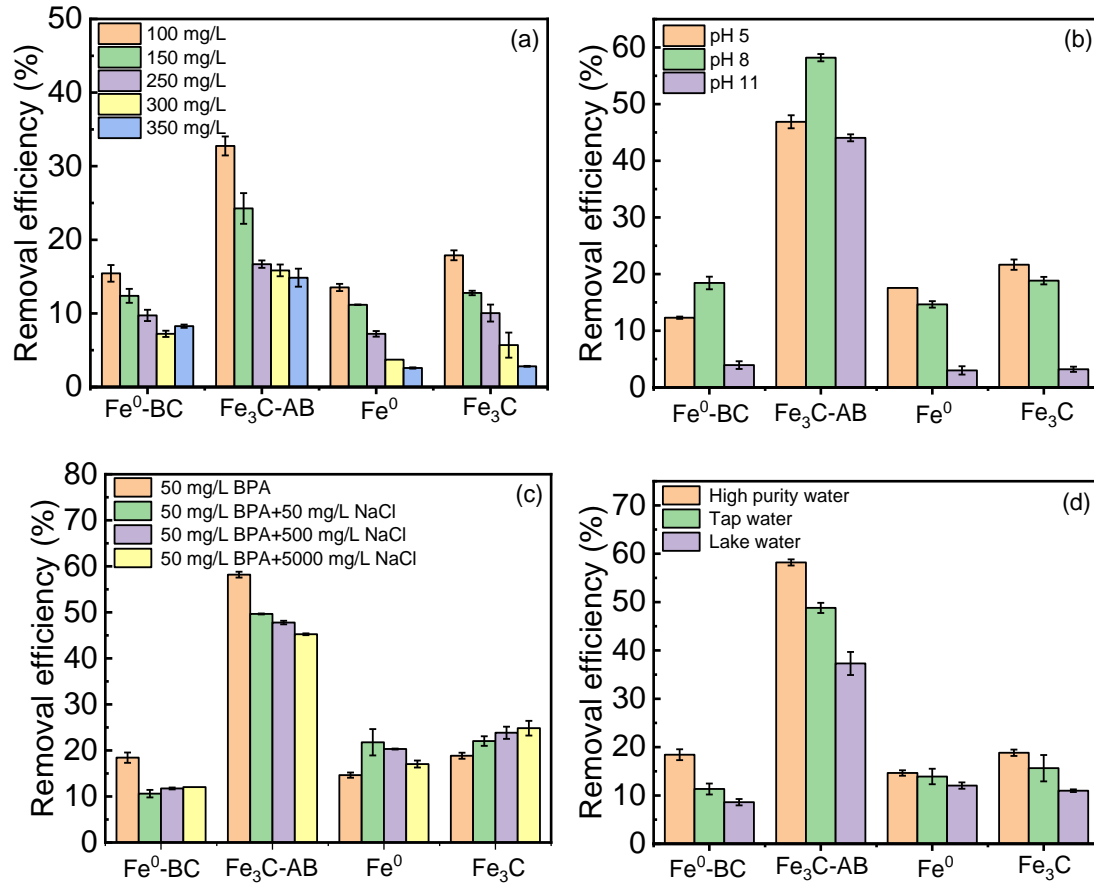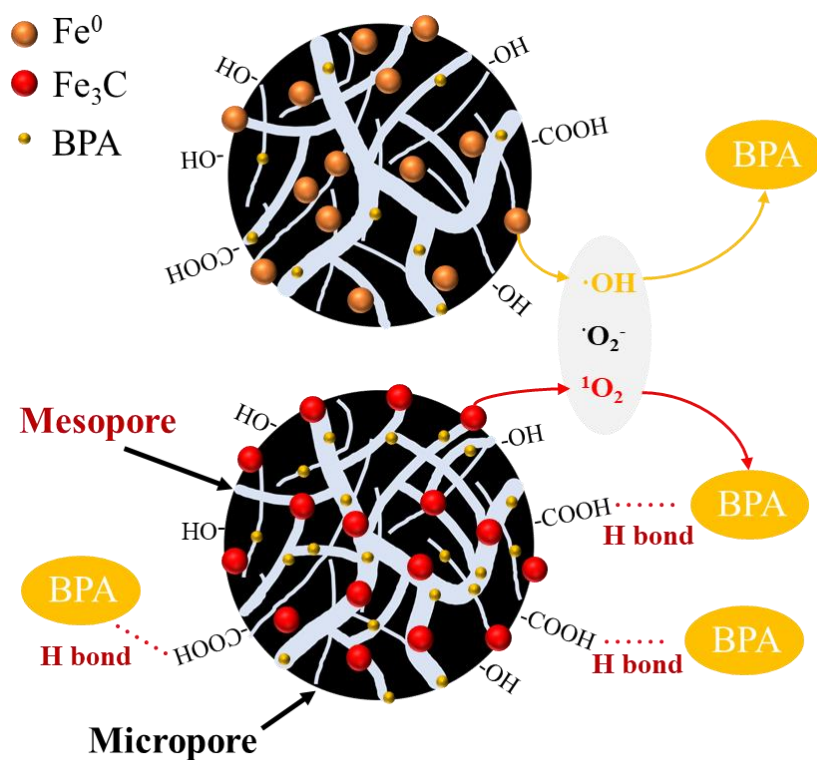
Fig. 4. The removal of BPA under (a) different initial concentration, (b) pH, (c) ion strength and (d) different kind of waters by Fe^0-BC, Fe$_3$C-AB, Fe^0 and Fe$_3$C at 24 h. The bars are standard deviation and all samples were run in duplicate.
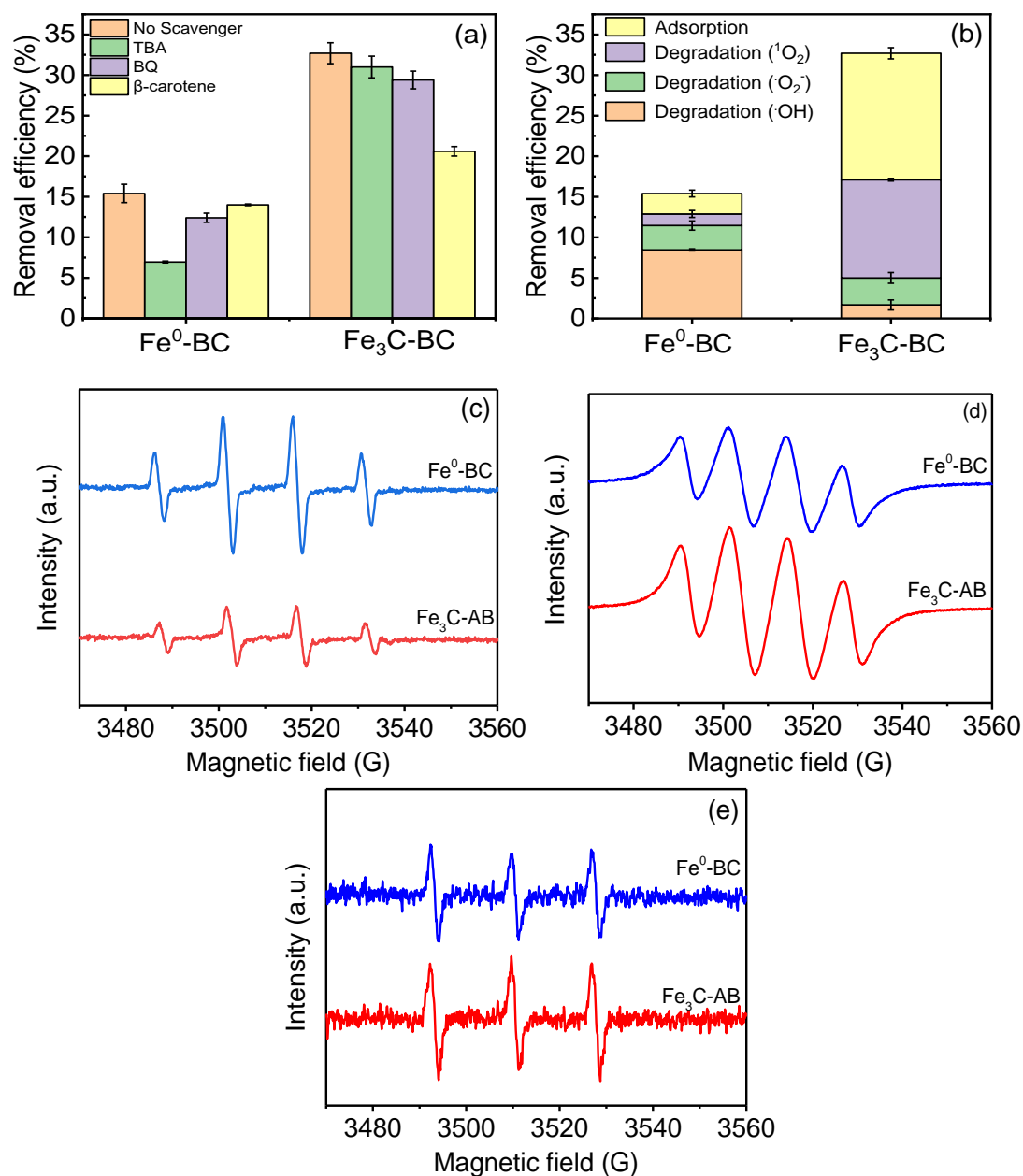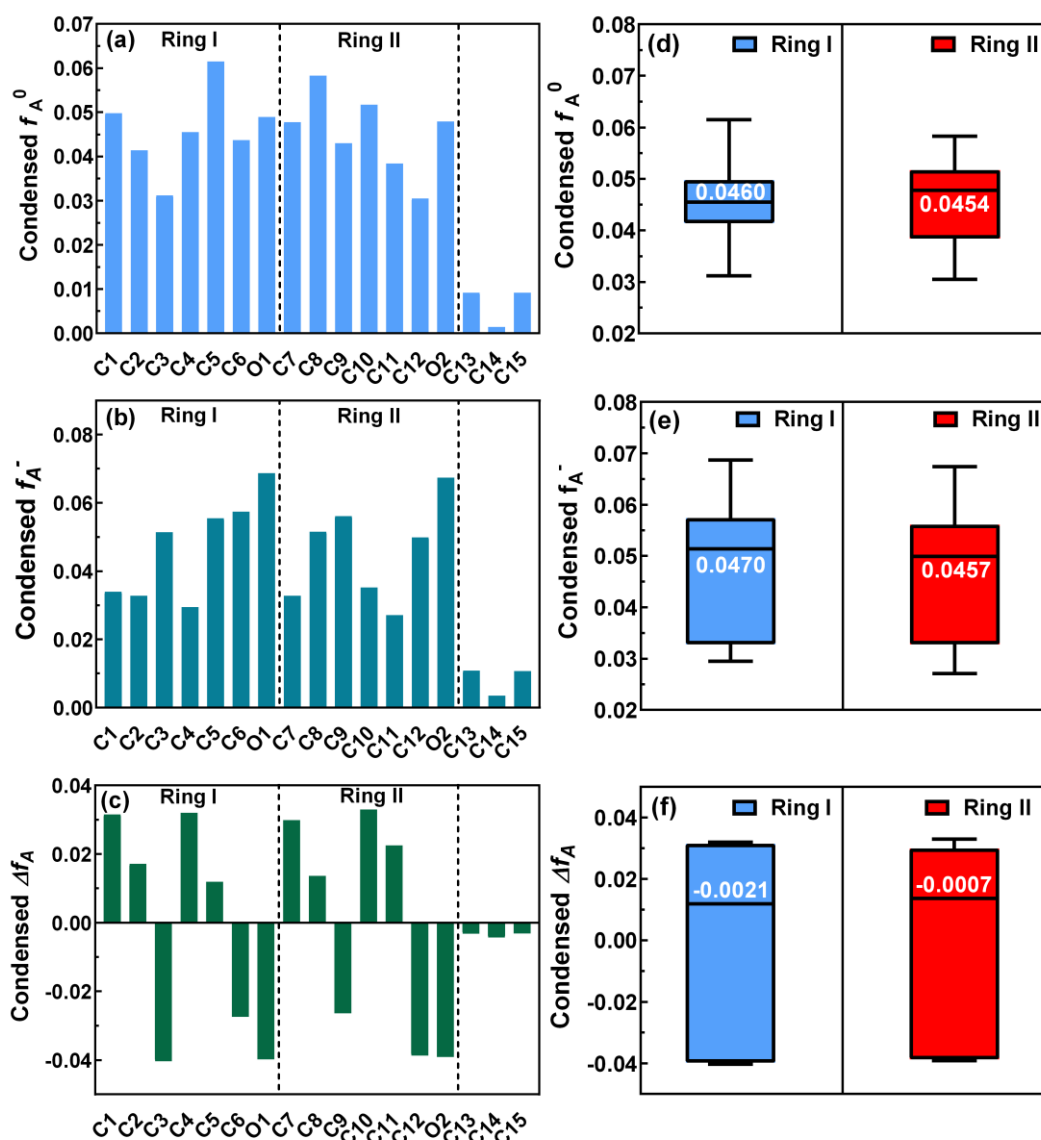
Fig. 5. (a) Effect of radical scavengers on BPA removal at 24 h. (b) Quantitative removal of BPA on different Fe/C composites by adsorption and degradation at 24 h. All samples were run in duplicate. DMPO spin-trapping spectra for (c) $\cdot OH$, (d) $\cdot O_2^-$ and TEMP spin-trapping spectra for (e) $^1O_2$ in different Fe/C composites. The bars are standard deviation. The experiment conditions were 100 mg/L initial concentration at pH 8, 25 ^{o}C from high purity water.

Fig. 6. Schematic representation of BPA removal mechanism by Fe/C composites.
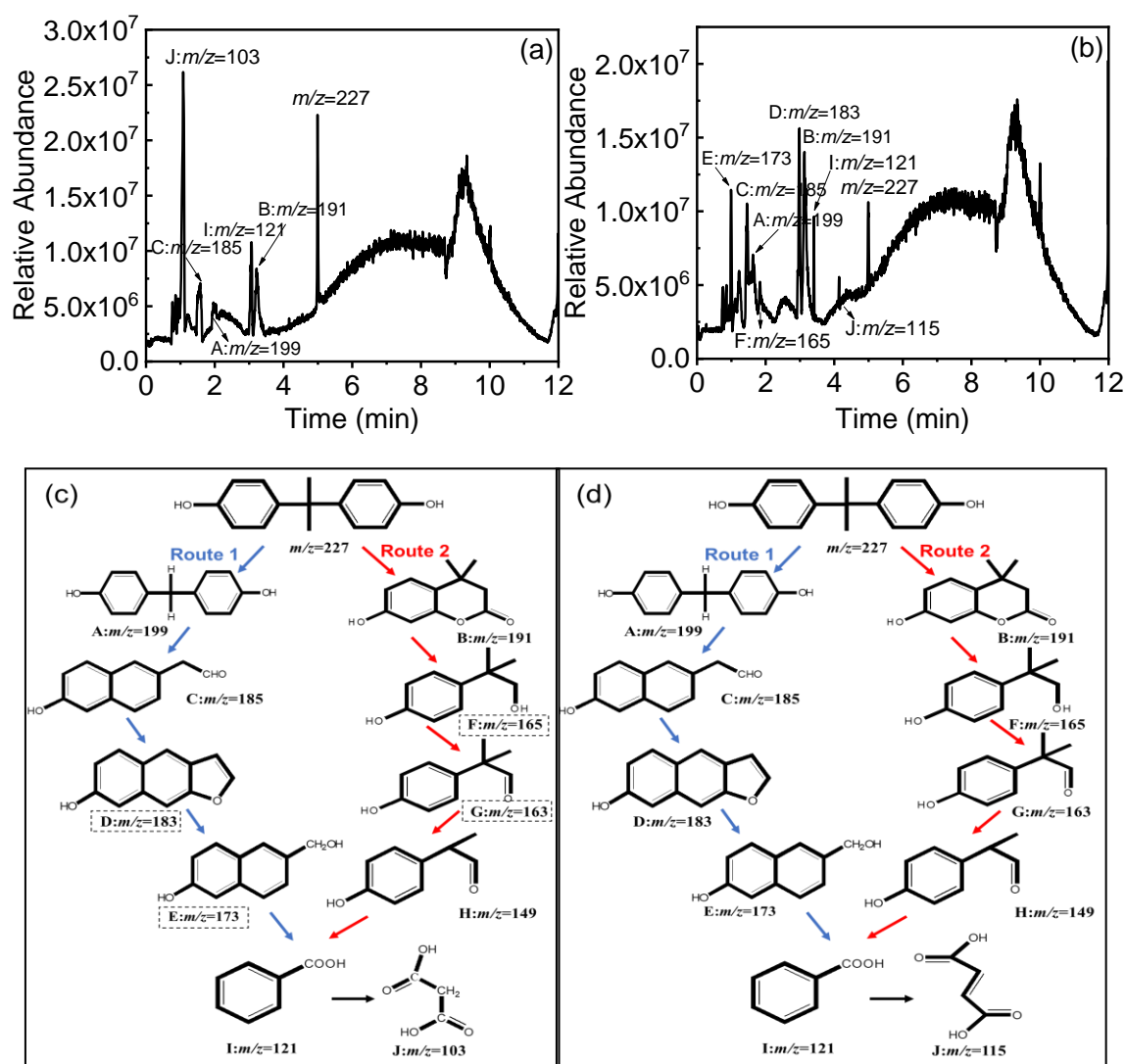
Fig. 7. Liquid chromatograph of BPA observed at 24 h for (a) Fe^0-BC and (b) Fe$_3$C-AB; Proposed degradation pathway of BPA by (c) Fe^0-BC and (d) Fe$_3$C-AB. Dotted square means the product was not detected in the solution, which might be adsorbed on the surface of Fe^0-BC. The experiment conditions were 50 mg/L initial concentration at pH 8, 25°C from high purity water.

Fig. 8. (a), (b), (c) condensed Fukui function f_A^0 and f_A^-, and condensed dual descriptors Δf_A value of C1–C15 and O1–O2; (d), (e), (f) box diagram of f_A^0, f_A^- and Δf_A value of ring I and ring II.